Activationless charge transport across 4.5 to 22 nm in molecular electronic junctions

Haijun Yan[a], Adam Johan Bergren[a], Richard McCreery[a,b,1], Maria Luisa Della Rocca[c], Pascal Martin[d], Philippe Lafarge[c], and Jean Christophe Lacroix[d]

[a]National Institute for Nanotechnology, Edmonton, AB, Canada T6G 2M9; [b]Department of Chemistry, University of Alberta, Edmonton, AB, Canada T6G 2G2; [c]Laboratoire Matériaux et Phénomènes Quantiques (MPQ), Unité Mixte de Recherche 7162, Centre National de la Recherche Scientifique (CNRS), Université Paris Diderot, Sorbonne Paris Cité, 75205 Paris Cedex 13, France; and [d]Laboratoire Interfaces, Traitements, Organisation et Dynamique des Systèmes (ITODYS), Unité Mixte de Recherche 7086, Centre National de la Recherche Scientifique (CNRS), Université Paris Diderot, Sorbonne Paris Cité, 75205 Paris Cedex 13, France

In this work, we bridge the gap between short-range tunneling in molecular junctions and activated hopping in bulk organic films, and greatly extend the distance range of charge transport in molecular electronic devices. Three distinct transport mechanisms were observed for 4.5–22-nm-thick oligo(thiophene) layers between carbon contacts, with tunneling operative when $d < 8$ nm, activated hopping when $d > 16$ nm for high temperatures and low bias, and a third mechanism consistent with field-induced ionization of highest occupied molecular orbitals or interface states to generate charge carriers when $d = 8$–22 nm. Transport in the 8–22-nm range is weakly temperature dependent, with a field-dependent activation barrier that becomes negligible at moderate bias. We thus report here a unique, activationless transport mechanism, operative over 8–22-nm distances without involving hopping, which severely limits carrier mobility and device lifetime in organic semiconductors. Charge transport in molecular electronic junctions can thus be effective for transport distances significantly greater than the 1–5 nm associated with quantum-mechanical tunneling.

all-carbon molecular junction | attenuation coefficient | field ionization | strong electronic coupling

Charge transport mechanisms in organic and molecular electronics underlie the ultimate functionality of a new generation of electronic devices. Understanding, controlling, and designing molecular devices for use as practical components requires an intimate knowledge of the system energy levels and operative transport mechanisms, and how key variables such as molecule length, identity, temperature, etc., affect device performance parameters. Especially interesting in this context is the relationship between organic electronic devices, which typically have active layer thicknesses of tens to hundreds of nanometers, and molecular electronic devices reported to date, in which at least one dimension for charge propagation is below 10 nm. Indeed, many types of functional organic electronic devices have been demonstrated, including thin-film transistors, organic light-emitting diodes, and memory cells (1, 2). Bridging the gap between organic and molecular devices may therefore reveal pathways for improving the performance of such devices, or even lead to new types of devices based on alternative transport mechanisms.

The great majority of molecular electronic devices investigated to date have transport distances of <5 nm between the contacts, where the prevalent transport mechanism is quantum-mechanical tunneling. For this distance range, there is general agreement that the conductance scales exponentially with length, with an attenuation coefficient (β), defined as the slope of ln J vs. thickness (d), equal to 8 to 9 nm^{-1} for aliphatic molecules (3–6) and 2–3 nm^{-1} for aromatic molecules (7–14). A few molecular electronic systems have been investigated beyond 5 nm (15, 16), some of which exhibit a decrease in β to less than 1 nm^{-1}. Such small values of β are significant both practically (17, 18) and fundamentally (19–22), because they imply transport across distances much greater than the dimensions of single molecules and may enable complex

molecular circuits. These low β-values are often dependent on temperature and have been attributed to activated hopping by a redox exchange mechanism (10, 23). However, phase-coherent tunneling has also been proposed for cases where the molecules have orbitals close in energy to the contact Fermi level (15, 24), resulting in minimal temperature dependence.

In this paper, we investigate the frontier between molecular and organic electronics by describing the electrical characteristics of conjugated molecular junctions of the structure carbon/molecule/carbon/Au over a wide range of thickness (from 4.5 to 22 nm). Reduction of a diazonium reagent of bis-thienylbenzene (BTB) (25–29) on carbon surfaces permits formation of molecular films of controlled thickness consisting of conjugated oligomers, and the electronic junction is completed by electron-beam deposition of carbon and gold (30). Such grafted oligo(BTB) layers can be easily p-doped and switched from insulating to conductive states in electrochemical conditions (25–28). Previous transport measurements in planar Au junctions containing a 7-nm–thick BTB molecular layer were explained with a mixed-transport mechanism combining a conducting molecular region with a tunnel barrier (31). In the present work, temperature and electrical field dependence of transport were analyzed to determine the likely transport mechanisms in three thickness regions: less than 8 nm, 8–16 nm, and greater than 16 nm. The results indicate three distinct transport mechanisms: coherent tunneling for $d < 8$ nm, activated hopping similar to that observed in bulk organic semiconductors for $d > 16$ nm, and a third mechanism which occurs over a broad range of temperature and electric field for molecular layer thicknesses of 8–22 nm.

Results and Discussion

Molecular junctions (area = 0.0013 cm^2) were constructed (9, 30, 32, 33) on pyrolyzed photoresist film (PPF), which is a flat, conducting sp^2 hybridized carbon surface described in detail previously (34). *SI Appendix,* Fig. S1 shows a junction schematic and the four-wire electronic apparatus used for device characterization; *SI Appendix,* sections 2 and 3 detail the fabrication procedure and thickness determination. Current density vs. voltage (JV) curves obtained for PPF/BTB/e-C/Au junctions with BTB thickness from 4.5 to 22 nm are shown in Fig. 1 A and C for linear and semilog J scales, respectively. Fig. 1 B and D shows a selection of the same devices collected at temperature (T) <10 K on linear (Fig. 1B) and semilog (Fig. 1D) scales. It is clear from analysis of these curves that: (i) J is nonlinear in V, but nearly symmetric with
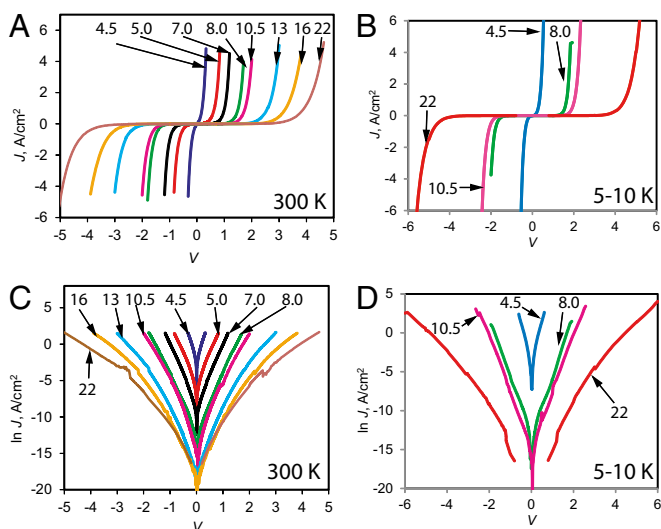
Fig. 1. Current density vs. voltage (*JV*) curves for PPF/BTB/e-C/Au molecular junctions with BTB layer thickness indicated on each curve in nanometers. In all cases, the top contact consisted of 10 nm of carbon (e-C) and 15 nm of Au deposited by electron-beam evaporation at ~5 × 10⁻⁷ torr. PPF is pyrolyzed photoresist film with covalent bonding to BTB layer, described previously (14, 34) (*SI Appendix, section 2*). *JV* curves were obtained with a four-wire geometry to correct for lead resistance. *A* and *C* were obtained at 300 K in air, whereas *B* and *D* were obtained at <10 K in vacuum.

respect to polarity; (*ii*) the slope of ln *J* vs. ln *V* approaches 1.0 at low *V*, but increases to 13–15 at high *V* (*SI Appendix*, Fig. S5 and Table S2); (*iii*) there is a strong dependence on thickness of the BTB layer; and (*iv*) there are no major changes in appearance or symmetry of the *JV* curves between high and low *T*.

To visualize the strong effect of thickness more directly, Fig. 2*A* displays room temperature attenuation plots (ln *J* vs. *d*) at three different bias voltages for all of the data in Fig. 1. The slope of the attenuation plot gives the value for β, a characteristic transport parameter that has been tied to transport mechanism, molecule identity, and other electronically relevant parameters such as conjugation length. There are three statistically distinguishable β-values identified from Fig. 2*A* (listed in *SI Appendix*, Table S3): β = 3.0 ± 0.3 nm⁻¹ (mean ± SD for *n* = 8) for *d* = 4–8 nm; β = 1.0 ± 0.2 nm⁻¹ (*n* = 19) for *d* = 8–16 nm; and β < 0.2 nm⁻¹ (*n* = 6) for *d* = 15–22. The values of β for *d* < 8 nm agree well with the 2–4 nm⁻¹ values reported for other aromatic molecules for this range of thickness (13, 14). Note that extrapolation of the ln *J* vs. *d* plot in the β = 3 nm⁻¹ region to *d* >8 nm (shown by the dashed line in

Fig. 2*A*) predicts current densities that are well below the observed values for *d* >8 nm, and *J* is predicted to decay below the detection limit at 0.3 V for *d* > 15 nm. This result clearly demonstrates that additional mechanisms must contribute for *d* > 8 nm. Previous studies using aromatic molecules have reported a transition from β ~ 3 nm⁻¹ to ~1 nm⁻¹ when *d* exceeds 4–5 nm (10, 23) This transition was attributed to a change in mechanism, with tunneling current dominant for the <4–5-nm region and thermally activated hopping for thicker layers. In these cases, the transition was accompanied by a change from temperature-independent current to measured activation barriers of 0.3–0.5 eV (10, 23, 35).

Fig. 2*B* shows an overlay of attenuation plots for BTB with a bias of +1 V obtained at five temperatures from 6 to 300 K. Importantly, for *d* < 8 nm both the value of β and the current magnitude are weakly dependent on temperature, consistent with transport controlled by quantum-mechanical tunneling, as previously reported for similar junctions (9, 30, 31). However, for the intermediate thickness range (8–12 nm), the current density decreases slowly with lower temperature, whereas β itself does not change significantly. This result indicates a low activation energy (described below), but also that the dominant transport mechanism in the β = 1.0 nm⁻¹ region is not strongly temperature dependent. For the thickness range of 16–22 nm, the attenuation factor β undergoes a shift from nearly zero to higher values at lower temperatures, approaching the β = 1 nm⁻¹ line extrapolated from *d* = 8–16 nm (Fig. 2*B*). Thus, for the thickest layers (>16 nm), there is an additional thermally activated transport mechanism with β < 0.2 nm⁻¹. *SI Appendix*, Fig. S4*B* shows direct overlap of the *JV* curves for 16 and 22 nm for low *V* and 300 K, confirming the small value of β. As discussed below, this additional current observed for *d* > 16 nm has characteristics of hopping, i.e., significant activation energy and weak distance dependence.

Fig. 3 *A* and *B* shows *JV* curves obtained from <10–300 K for 10.5- and 22-nm BTB junctions (*d* = 4.5 and 8.0 nm are shown in *SI Appendix*, Fig. S6). Arrhenius plots derived from *JV* curves at several bias values are shown in Fig. 3 *C* and *D*, and Table 1 provides activation barrier energies (E_a) derived from Arrhenius slopes as a function of bias, temperature range, and BTB thickness. In most cases, there are two linear sections: a high-temperature region with E_a > 100 meV and a low-temperature region with much smaller E_a, usually <25 meV. Several observations, which bear directly on the transport mechanism(s), are possible by analyzing data in Table 1 and Fig. 3. First, E_a is <0.5 meV for all thicknesses and voltages in the temperature range from 5 to 50 K. Second, the higher E_a values (150–300 meV) are observed in the high-thickness regime (*d* = 16–22 nm) for *T* = 200–300 K and low *V* where β ~ 0. Moreover, for this regime the E_a decreases sharply with increasing bias voltage. Third, E_a values of 26–85 meV with weaker *T* dependence are observed in the same temperature range for *d* = 8.0 and 10.5 nm.

We now consider the electrical characteristics of the thicker junctions (*d* = 8–22 nm) in conditions where β ~ 0 or 1 nm⁻¹ to assess possible transport mechanisms. Temperature-dependent transport with a small β-value has been associated with activated hopping between sites in both single molecules (35, 36) and ensemble junctions (16, 23), presumably governed by Marcus–Levich kinetics. The low-*V*, high-*T* Arrhenius slopes of 150–300 meV listed in Table 1 are comparable to those reported for bulk polythiophene, e.g., 128–143 meV (37) and 280 meV (38), in which interchain charge transfer dominates transport (39, 40). The additional thermally activated transport mechanism that provides an extra current contribution and yields the β = 0 nm⁻¹ values seen in BTB devices at room temperature can thus be attributed to redox hopping, and represents the bulk limit commonly observed in organic semiconductors. However, for either high *V* or low *T*, the activated character of transport is diminished, indicating a change in mechanism. Regardless of the
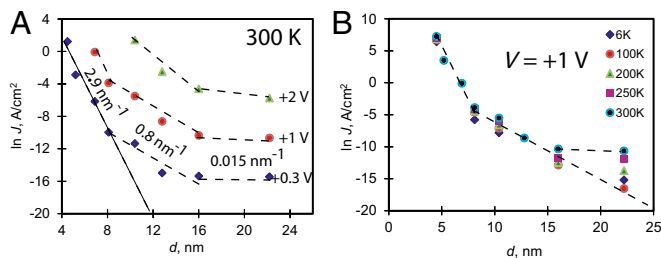

Fig. 2. (*A*) Attenuation plots (ln *J* vs. *d*) at three bias values indicated, obtained at 300 K in air. (*B*) Attenuation plots obtained at *V* = +1 V at the indicated temperatures between 6 and 300 K, all in vacuum. Linear regions with three different slopes are indicated by dashed lines. In two instances (4.5 and 5.2 nm at 300 K) in *B*, the current was too high to be measured at 1 V; these data points were obtained by extrapolating curves obtained at 0.5 to 1 V. SDs for similar devices are <25% in *J* and ±0.6 nm in thickness (9, 14, 30).
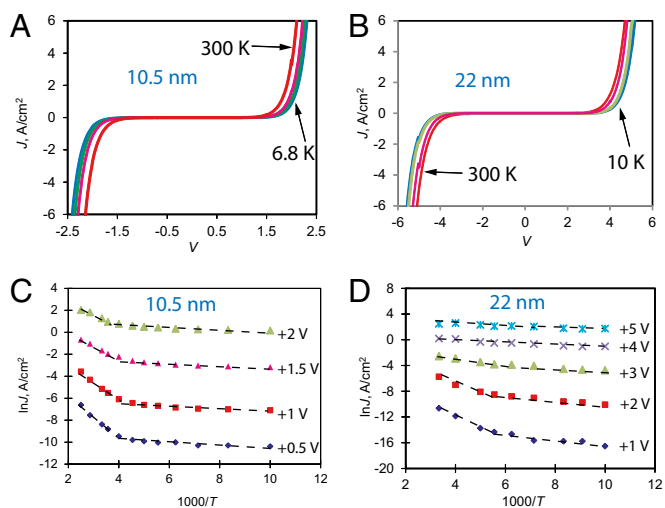
Fig. 3. JV curves at <10, 100, 200, and 300 K for (A) 10.5- and (B) 22-nm junctions. Arrhenius plots of ln J vs. 1000/T for (C) 10.5- and (D) 22.2-nm BTB junctions, obtained at the indicated bias values. Linear portions are identified by dashed lines, and a complete listing of E_a appears in Table 1. *SI Appendix*, Fig. *S8A* shows the dependence of E_a on bias.

origin of such behavior, an important and exciting consequence is the possibility of long distance, activationless charge transport across distances not possible with coherent tunneling.

Several classical mechanisms possible in molecular junctions in addition to tunneling and hopping include thermionic (i.e., Schottky) emission, field ionization (i.e., Fowler–Nordheim, or FN, tunneling), Poole–Frenkel (PF) transport between Coulombic traps, and variable range hopping (VRH). Of these, FN tunneling is independent of temperature, and is predicted to yield a linear plot of ln (J/E^2) vs. $1/E$ (i.e., an FN plot), where E is the electric field (41, 42). Fig. 4A shows an overlay of FN plots of BTB

Table 1. Arrhenius slopes for varying thickness and bias

		E_a, meV		
d, nm	V	5–50 K	100–200 K	200–300 K
4.5	0.1	0.16	9	30
	0.2	0.12	6	24
	0.5	0.1		
8.0	0.2	0.28	5	26
	0.5	0.12	4	39
	1.0	0.04	4	48
	1.5	0.08	3	43
10.5	0.2	0.15	13	85
	0.5	0.43	8	79
	1.0	0.01	8	75
	1.5	0.1	8	54
	2.0	0.08	6	36
16	0.2			291
	0.5		10	209
	1.0		5	175
	1.5		2	130
	2.0		2	99
	3.0		1	60
22	1.0	0.26	43	160
	2.0	0.43	33	119
	3.0	0.34	22	47
	4.0	0.09	13	28
	5.0	0.03	10	9

junctions as a function of BTB thickness at 300 K. Note that the curves for $d = 8.0$, 10.5, and 22 nm converge at high field, implying that transport is controlled by electric field above $E = 1$ MV/cm. Fig. 4B shows the same plot for the 8.0- and 22-nm thicknesses at 6 and 300 K. It is clear that the curves converge at high E for both temperatures, but do not exhibit the linear region predicted from FN theory. VRH is characterized by a linear plot of ln J vs. $T^{-1/4}$ for three-dimensional Mott VRH or ln J vs. or $T^{-1/2}$ for one-dimensional Mott VRH or Efros–Shklovskii VRH (43–45). Several such plots are shown in *SI Appendix*, Fig. *S7*, and exhibit no linear regions for the temperature dependence shown in Fig. 3. We conclude that neither VRH nor FN mechanisms are consistent with the JV results over the entire temperature and bias ranges examined. PF and Schottky mechanisms predict linearity of ln (J/E) vs. $E^{1/2}$, and such plots are shown in Fig. 4C at 300 K and Fig. 4D for < 10 K. The curves for $d = 8.0$–22 nm converge at high E at both temperatures, and the low-T case shows excellent linearity of ln (J/E) vs. $E^{1/2}$, especially for $d = 22$ nm for which $R^2 = 0.9989$ over 8 orders of magnitude of J/E. Both mechanisms also predict linearity of E_a vs. $E^{1/2}$ with intercepts at zero field equal to the barrier height. Such plots are shown in *SI Appendix*, Fig. *S8A*, exhibiting reasonable linearity for 16- and 22-nm junctions for the 200- to 300-K Arrhenius slopes, and intercepts at zero field indicating barrier heights of ~350 meV (16 nm) and ~300 meV (22 nm). These results indicate that PF or Schottky mechanisms may be valid above 200 K for $d \geq 16$ nm, where a voltage-dependent E_a is observed (Table 1). PF transport has been proposed for organic semiconductors across distances greater than studied here, and is consistent with observed E dependence (46–49).

However, PF and Schottky mechanisms are not consistent with the weak temperature dependence below 200 K. Comparing Fig. 4 C and D, the experimental curves are very similar for 300 K and <10 K, contrary to the predictions of Schottky and PF equations for ~300-meV barriers. As shown in *SI Appendix*, Fig. *S8B*, the slope of the experimental ln (J/E) vs. $E^{1/2}$ plot increases by a factor of 1.32 between 300 and 6 K for $d = 22$ nm, although theory predicts it should increase by a factor of >50 (300/6) for either PF or Schottky mechanisms. We conclude that classical Schottky or PF transport cannot explain transport in BTB junctions, nor can the FN or VRH models discussed above. Therefore, there must be another mechanism operative below 200 K which becomes dominant at
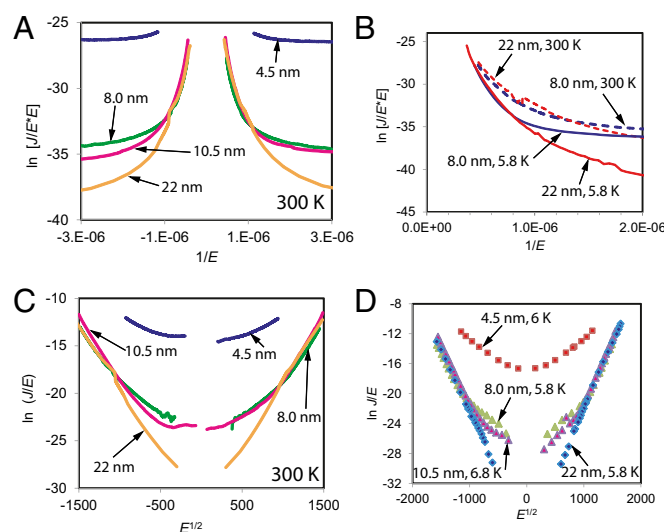

Fig. 4. (A) FN plot of ln (J/E^2) vs. $1/E$, where E = electric field (V/cm) at 300 K for the indicated BTB thicknesses. (B) FN plot for 8.0- and 22-nm BTB devices at <5.8 and 300 K. (C and D) PF plots of ln (J/E) vs. $E^{1/2}$ for the same four BTB thicknesses at (C) 300 and (D) <10 K.

Yan et al.

moderate and high electric field. This mechanism has not been reported previously for molecular junctions, and is temperature independent with a β of ~1.0 nm^{-1} for BTB junctions with $d = 8$–22 nm, as shown in Fig. 2.

Given that classical mechanisms are not consistent with the BTB JV behavior, we note a few recent observations of field-driven mechanisms for transport in much thicker organic films (>100 nm) (46–49). Whereas transport dimensions and bias voltages were much larger than the 4.5–22-nm range studied here, a linear dependence of ln J vs. $E^{1/2}$ was observed, as was T-independent conductance at low T. Although the mechanism is controversial, these observations were attributed to field-assisted hopping (46, 48), field-assisted tunneling (47, 48), multistep tunneling (47), or behavior similar to a Luttinger liquid (49). For the case of polythiophene thin-film transistors, a transition from PF-like behavior at room temperature to temperature-independent field-emission hopping with an $E^{1/2}$ dependence at low temperature was reported (48).

In the present case, to explain transport in the region where β ~ 1.0 nm^{-1}, we propose that field ionization occurs when the stabilization energy of an electron in the applied field exceeds the trap depth, similar to PF transport. The "trap" could be a localized state such as the highest occupied molecular orbital (HOMO) of oligo (BTB) or a hybrid orbital that has density on both the molecule and the contact, such as a "gap state" (50). Such hybrid states are likely in a system with a covalently bonded molecular layer, which is known to induce Fermi-level pinning and strong electronic coupling (14, 50). The distinction between classical PF behavior and the proposed field ionization mechanism lies in the events following ionization. Conventional activated PF transport involves thermal carrier generation assisted by the applied field, and subsequent transport characterized by the mobility of the carriers. The very short transport distances in the BTB junctions may permit ballistic carrier transport following ionization, such that ionization and transport are concerted. Rapid refilling of the field-ionized orbital from one electrode would permit further ionization and current flow with no need for reorganization, thus maintaining activationless transport. An additional possibility after the initial field-ionization event is relaxation of the ionized centers to form polarons, resulting in new conduction channels with high conductivity. Such polarons are expected to be 5–10 nm long, and are

therefore comparable to the thickness of several of the BTB junctions studied, so that a single intrachain transfer is sufficient for charge transport within the molecular layer (51, 52). Such intrachain transport is expected to have activation energies in the 40–80-meV range (51), consistent with some of the low observed E_a values.

Conclusions

Charge transport in 4.5–22-nm BTB molecular junctions is characterized by three attenuation factors and three distinct mechanisms. For $d < 8$ nm, current is controlled by coherent tunneling, with minimal temperature dependence and β = 3 nm^{-1}, as described previously for conjugated molecular junctions (9, 14, 30). For low field and high T, the thickest devices ($d > 16$ nm) exhibit hopping transport with β < 0.1 nm^{-1} and strong T dependence, similar to that observed for bulk organic semiconductors. For a wide range of thickness (8–22 nm) and T (6–300 K), a third, nearly activationless mechanism with β ~ 1 nm^{-1} and E_a between 0 and 80 meV is observed, for which the current is controlled mainly by the electric field. This mechanism is consistent with field-induced ionization of molecular HOMOs or interface states to generate charge carriers. The field required for onset of ionization is presumably dependent on the energy of the orbital to be ionized relative to the system Fermi level. Following ionization, the empty state may be rapidly refilled from the negatively biased electrode, or may reorganize to form a polaron and a new conducting channel. Activated hopping is important for thicker films at high T and low electric field, whereas field ionization becomes dominant at high electric field and all temperatures examined. In addition to identifying an additional transport mechanism for molecular junctions, the current report unifies the fields of molecular and organic electronics by covering distances from short-range tunneling to activated, long-range hopping which underlies transport in bulk organic semiconductors.

1. Naber WJM, Faez AS, van der Wiel AWG (2007) Organic spintronics. *J Phys D Appl Phys* 40(12):R205–R228.
2. Scott JC, Bozano LD (2007) Nonvolatile memory elements based on organic materials. *Adv Mater (Deerfield Beach Fla)* 19(11):1452–1463.
3. Akkerman HB, De Boer B (2008) Electrical conduction through single molecules and self-assembled monolayers. *J Phys Condens Matter* 20:013001.
4. Bonifas AP, McCreery RL (2010) 'Soft' Au, Pt and Cu contacts for molecular junctions through surface-diffusion-mediated deposition. *Nat Nanotechnol* 5(8):612–617.
5. Bonifas AP, McCreery RL (2011) Assembling molecular electronic junctions one molecule at a time. *Nano Lett* 11(11):4725–4729.
6. Weiss EA, et al. (2007) Influence of defects on the electrical characteristics of mercury-drop junctions: Self-assembled monolayers of n-alkanethiolates on rough and smooth silver. *J Am Chem Soc* 129(14):4336–4349.
7. Kronemeijer AJ, et al. (2010) Electrical characteristics of conjugated self-assembled monolayers in large-area molecular junctions. *Appl Phys Lett* 97(17):173302.
8. Anariba F, Steach JK, McCreery RL (2005) Strong effects of molecular structure on electron transport in carbon/molecule/copper electronic junctions. *J Phys Chem B* 109(22):11163–11172.
9. Bergren AJ, McCreery RL, Stoyanov SR, Gusarov S, Kovalenko A (2010) Electronic characteristics and charge transport mechanisms for large area aromatic molecular junctions. *J Phys Chem C* 114(37):15806–15815.
10. Ho Choi S, Kim B, Frisbie CD (2008) Electrical resistance of long conjugated molecular wires. *Science* 320(5882):1482–1486.
11. Engelkes VB, Beebe JM, Frisbie CD (2004) Length-dependent transport in molecular junctions based on SAMs of alkanethiols and alkanedithiols: Effect of metal work function and applied bias on tunneling efficiency and contact resistance. *J Am Chem Soc* 126(43):14287–14296.
12. Liu H, et al. (2008) Length-dependent conductance of molecular wires and contact resistance in metal-molecule-metal junctions. *ChemPhysChem* 9(10):1416–1424.
13. Salomon A, et al. (2003) Comparison of electronic transport measurements on organic molecules. *Adv Mater (Deerfield Beach Fla)* 15(22):1881–1890.

14. Sayed SY, Fereiro JA, Yan H, McCreery RL, Bergren AJ (2012) Charge transport in molecular electronic junctions: Compression of the molecular tunnel barrier in the strong coupling regime. *Proc Natl Acad Sci USA* 109(29):11498–11503.
15. Sedghi G, et al. (2012) Comparison of the conductance of three types of porphyrin-based molecular wires: β,meso,β-fused tapes, meso-Butadiyne-linked and twisted meso-meso linked oligomers. *Adv Mater (Deerfield Beach Fla)* 24(5):653–657.
16. Tuccitto N, et al. (2009) Highly conductive approximately 40-nm-long molecular wires assembled by stepwise incorporation of metal centres. *Nat Mater* 8(1):41–46.
17. DiBenedetto SA, Facchetti A, Ratner MA, Marks TJ (2009) Charge conduction and break-down mechanisms in self-assembled nanodielectrics. *J Am Chem Soc* 131(20):7158–7168.
18. Goldsmith RH, et al. (2008) Unexpectedly similar charge transfer rates through benzo-annulated bicyclo[2.2.2]octanes. *J Am Chem Soc* 130(24):7659–7669.
19. Berlin YA, Grozema FC, Siebbeles LDA, Ratner MA (2008) Charge transfer in donor-bridge-acceptor systems: Static disorder, dynamic fluctuations, and complex kinetics. *J Phys Chem C* 112(29):10988–11000.
20. Lindsay SM, Ratner MA (2007) Molecular transport junctions: Clearing mists. *Adv Mater (Deerfield Beach Fla)* 19(1):23–31.
21. Mujica V, Kemp M, Ratner MA (1994) Electron conduction in molecular wires. I. A scattering formalism. *J Chem Phys* 101(8):6849–6855.
22. Mujica V, Kemp M, Ratner MA (1994) Electron conduction in molecular wires. II. Application to scanning tunneling microscopy. *J Chem Phys* 101(8):6856–6864.
23. Choi SH, et al. (2010) Transition from tunneling to hopping transport in long, conjugated oligo-imine wires connected to metals. *J Am Chem Soc* 132(12):4358–4368.
24. Sedghi G, et al. (2011) Long-range electron tunnelling in oligo-porphyrin molecular wires. *Nat Nanotechnol* 6(8):517–523.
25. Fave C, et al. (2007) Tunable electrochemical switches based on ultrathin organic films. *J Am Chem Soc* 129(7):1890–1891.
26. Fave C, et al. (2008) Electrochemical switches based on ultrathin organic films: From diode-like behavior to charge transfer transparency. *J Phys Chem C* 112(47):18638–18643.
27. Santos L, Ghilane J, Lacroix JC (2012) Formation of mixed organic layers by stepwise electrochemical reduction of diazonium compounds. *J Am Chem Soc* 134(12):5476–5479.

CHEMISTRY

28. Santos L, et al. (2010) Host-guest complexation: A convenient route for the electro-reduction of diazonium salts in aqueous media and the formation of composite materials. *J Am Chem Soc* 132(5):1690–1698.
29. Stockhausen V, et al. (2009) Grafting oligothiophenes on surfaces by diazonium electroreduction: A step toward ultrathin junction with well-defined metal/oligomer interface. *J Am Chem Soc* 131(41):14920–14927.
30. Yan H, Bergren AJ, McCreery RL (2011) All-carbon molecular tunnel junctions. *J Am Chem Soc* 133(47):19168–19177.
31. Martin P, Della Rocca ML, Anthore A, Lafarge P, Lacroix J-C (2012) Organic electrodes based on grafted oligothiophene units in ultrathin, large-area molecular junctions. *J Am Chem Soc* 134(1):154–157.
32. Bergren AJ, Harris KD, Deng F, McCreery RL (2008) Molecular electronics using di-azonium-derived adlayers on carbon with Cu top contacts: Critical analysis of metal oxides and filaments. *J Phys Condens Matter* 20(37):374117.
33. Mahmoud AM, Bergren AJ, Pekas N, McCreery RL (2011) Towards integrated molec-ular electronic devices: Characterization of molecular layer integrity during fabrica-tion processes. *Adv Funct Mater* 21(12):2273–2281.
34. Ranganathan S, McCreery RL, Majji SM, Madou M (2000) Photoresist-derived carbon for microelectrochemical applications. *J Electrochem Soc* 147(1):277–282.
35. Hines T, et al. (2010) Transition from tunneling to hopping in single molecular junc-tions by measuring length and temperature dependence. *J Am Chem Soc* 132(33):11658–11664.
36. Lee SK, et al. (2012) Universal temperature crossover behavior of electrical conduc-tance in a single oligothiophene molecular wire. *ACS Nano* 6(6):5078–5082.
37. Goh C, Kline RJ, McGehee MD, Kadnikova EN, Frechet JMJ (2005) Molecular-weight-dependent mobilities in regioregular poly(3-hexyl-thiophene) diodes. *Appl Phys Lett* 86(12):122110–122113.
38. Nolasco JC, et al. (2010) Extraction of poly (3-hexylthiophene) (P3HT) properties from dark current voltage characteristics in a P3HT/n-crystalline-silicon solar cell. *J Appl Phys* 107(4):044505.
39. Jiang X, et al. (2001) Mobilities of charge carriers hopping between [small pi]-conjugated polymer chains. *J Mater Chem* 11(12):3043–3048.
40. Cornil J, Beljonne D, Calbert JP, Brédas JL (2001) Interchain interactions in organic π-conjugated materials: Impact on electronic structure, optical response, and charge transport. *Adv Mater (Deerfield Beach Fla)* 13(14):1053–1067.
41. Aswal DK, Lenfant S, Guerin D, Yakhmi JV, Vuillaume D (2005) Fowler-Nordheim tunnelling and electrically stressed breakdown of 3-mercaptopropyltrimethoxysilane self-assembled monolayers. *Nanotechnology* 16(12):3064–3068.
42. Sze SM, ed (1981) *Physics of Semiconductor Devices*, 2nd Ed (Wiley, New York).
43. Hill RM (1976) Variable-range hopping. *Phys Status Solidi* 34:601–613.
44. Jang EY, et al. (2012) Fibers of reduced graphene oxide nanoribbons. *Nanotechnol-ogy* 23(23):235601.
45. Mott NF, Davis EA (1979) *Electronic Processes in Non-Crystalline Materials* (Clarendon, Oxford).
46. Prigodin VN, Epstein AJ (2007) Comment on "Voltage-induced metal-insulator tran-sition in polythiophene field-effect transistors." *Phys Rev Lett* 98(25):259703.
47. Wei JH, Gao YL, Wang XR (2009) Inverse square-root field dependence of conductivity in organic field-effect transistors. *Appl Phys Lett* 94(7):073301.
48. Worne JH, Anthony JE, Natelson D (2010) Transport in organic semiconductors in large electric fields: From thermal activation to field emission. *Appl Phys Lett* 96(5):53308.
49. Yuen JD, et al. (2009) Nonlinear transport in semiconducting polymers at high carrier densities. *Nat Mater* 8(7):572–575.
50. Braun S, Salaneck WR, Fahlman M (2009) Energy-level alignment at organic/metal and organic/organic interfaces. *Adv Mater (Deerfield Beach Fla)* 21(14–15):1450–1472.
51. Lacroix JC, Chane-Ching KI, Maquère F, Maurel F (2006) Intrachain electron transfer in conducting oligomers and polymers: The mixed valence approach. *J Am Chem Soc* 128(22):7264–7276.
52. Geskin VM, Dkhissi A, Brédas JL (2003) Oligothiophene radical cations: Polaron structure in hybrid DFT and MP2 calculations. *Int J Quantum Chem* 91(3):350–354.

Supporting Information for:

Activationless Charge Transport across 4.5 to 22 nm in Molecular Electronic Junctions

Haijun Yan[a], Adam Johan Bergren[a], Richard L. McCreery[a,b] *

Maria Luisa Della Rocca[c], Pascal Martin[d], Philippe Lafarge[c], Jean Christophe Lacroix[d]

a. National Institute for Nanotechnology, Edmonton, AB, Canada T6G 2M9; b. Department of Chemistry, University of Alberta, Edmonton, AB, Canada T6G 2G2; c. Laboratoire Matériaux et Phénomènes Quantiques (MPQ), Unité Mixte de Recherche 7162, Centre National de la Recherche Scientifique (CNRS), Université Paris Diderot, Sorbonne Paris Cité, 75205 Paris Cedex 13, France; d. Laboratoire Interfaces, Traitements, Organisation et Dynamique des Systèmes (ITODYS), Unité Mixte de Recherche 7086, Centre National de la Recherche Scientifique (CNRS), Université Paris Diderot, Sorbonne Paris Cité, 75205 Paris Cedex 13, France

 Contents:

1. Experimental Schematics

2. Junction fabrication

3. Measurement of Molecular Layer Thickness and Microscopy

4. Representative Current-Voltage results

5. Plots of ln J vs ln$V$

6. Attenuation coefficients (β) for various conditions

7. Supplemental JV curves for T = 6-300 K range

8. Variable Range Hopping plots

9. Activation barrier dependence on electric field

1. Experimental schematics

Figure S1A shows a schematic cross section of the all-carbon molecular junction, consisting of oligomers of bis-thienyl-benzene (BTB) between a carbon substrate and a carbon top contact. The molecular layer is partially ordered with covalent bonding to the PPF substrate, and has a range of thickness from 4.5 to 22 nm. Figure S1B shows an image of the top of two completed junctions, which occur at the intersection of orthogonal lines of PPF and top contact, along with three of the four probes used to make electrical contact. Figure S1C is a schematic of the 4-wire circuit used for current/voltage measurements, which compensates for lead and probe contact resistances. Junction area was 0.00125 cm^2 in all cases.
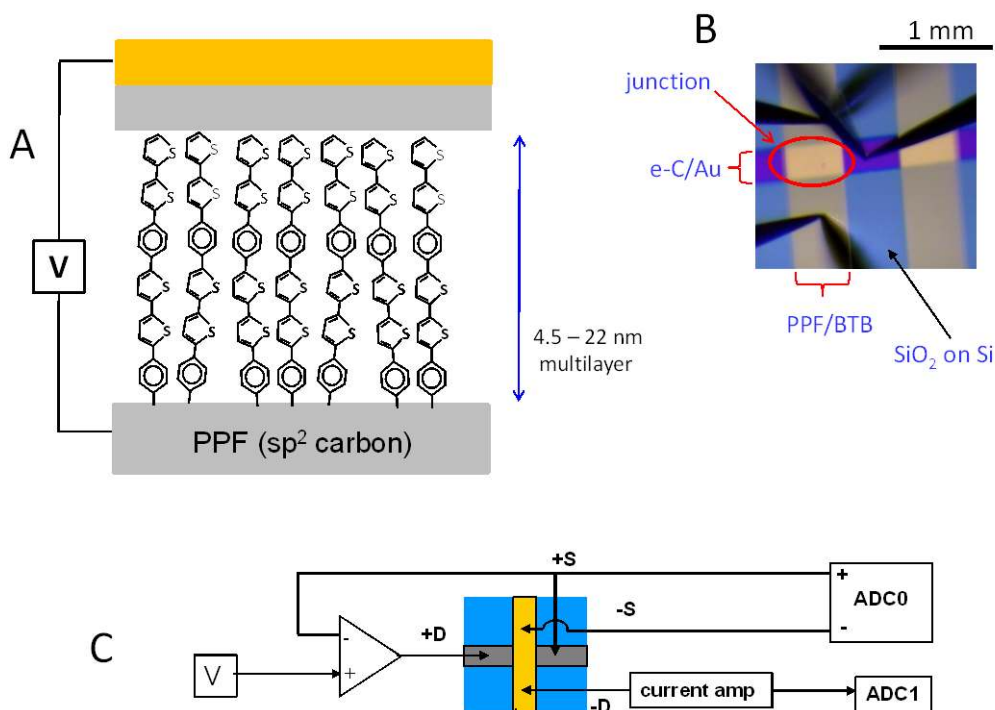
Figure S1A. Junction schematic (A), image of completed junction from above, showing three of the four contact probes (B), and electronic schematic of 4-wire system used for JV measurements (C). ADC0 and ADC1 are inputs to a National Instruments 6111 data acquisition board, and the "current amp" is a Stanford Research Systems 570 current amplifier. Applied voltage (V) is provided by DAC0 from the 6111 board, and was scanned at 1000 V/sec in most cases. For currents < 200 nA which occurred at low bias a Keithley 6517B electrometer in two electrode configuration was used to measure a series of discrete bias values.

I-V curves were measured by different methods depending on the thickness of the molecular layer. Thus, for thin layers where capacitive current is small, voltage scans were used, typically at 100 or 1000 V/s. As the thickness and capacitive current increased, the DC characteristic was obtained by either slowing the scan rate to as low as 0.5 V/s, or by a series of DC voltage pulses. In the latter case, voltage pulses were applied every 0.1 V or so, and the capacitive current was allowed to decay prior to taking a current reading.

2. Junction Fabrication

The "crossed junction" design has been reported in a series of papers (1-10), and was used here with bis-thienyl benzene (BTB) as the molecular component, a substrate of pyrolyzed photoresist film (PPF) (11) and a top contact of electron-beam deposited carbon (e-C) and Au. Preparation of PPF has been described in detail previously (1, 11), but consists of photolithographic patterning of four parallel 0.5 mm wide lines of photoresist on Si/SiO$_2$ surfaces followed by pyrolysis in a flowing H$_2$/N$_2$ atmosphere at 1100 ^{o}C. The result is four conducting, sp^2 hybridized carbon "stripes" with surface roughness < 0.4 nm rms.

The precursor to the BTB diazonium reagent, 1-(bithien-2-yl)-4-aminobenzene [BTAB] was prepared as described previously (4), then its diazonium ion was prepared in-situ before electrochemical modification of PPF as follows: An acetonitrile (ACN) solution (20 mL) containing BTAB (5mM, ~2.6mg) and tetrabutylammonium tetrafluoroborate (TBABF$_4$, 0.1M, ~0.66g) as supporting electrolyte was prepared and degassed with high purity argon for ~30 minutes. Tert-butylnitrite (36μL) was then added to the above solution and was stirred for 15 min before electrografting was started. Electrografting was carried out with cyclic voltammetry in the above solution using PPF as working electrode, Ag/Ag+ as reference electrode and Pt as counter electrode. Cyclic voltammetric sweeps were initiated from +400 mV to selected negative potentials at 100 mV/s. Various thicknesses were obtained by varying the negative potential range and number of scans, as noted in table S1. After surface modification, samples were thoroughly rinsed with copious ACN and dried with Ar. Typical values for the surface roughness (rms) determined with tapping-mode AFM were 0.4 nm for bare PPF and 0.5 nm for a 10.5nm BTB film on PPF. After electrografting, orthogonal lines (250 μm wide) of 10 nm e-C and 15 nm Au were applied to the PPF/BTB "stripes" through a shadow mask by electron-beam deposition, as described previously (7). Raman spectroscopy of similar PPF/molecule/e-C/Au junctions through both the top contact and a transparent substrate before and after e-C/Au deposition revealed no observable structural changes to the molecular layer during top contact deposition (5, 7, 12).

3. Measurement of Molecular Layer Thickness and Microscopy

Oligo-BTB film thicknesses on PPF were determined by an Atomic Force Microscopy (AFM) "scratching" technique described previously (6, 13). Thickness measurements were carried out on PPF/BTB immediately adjacent to one of the junctions of each sample. First, contact mode was applied to scratch a trench (1 x 1 µm) in the molecular layer, with the result shown in figure S2A. A set point (0.25V) was used to remove the molecules but not damage the underlying PPF substrate. A 5 x 5 µm tapping-mode image was then obtained in the area surrounding and including the trench. Finally, the image was analyzed within the area defined by the white rectangle in Figure S2A to determine the difference in height between the bottom of the trench and the upper surface of the molecular layer. A histogram generated from the height data was fit by two separate Gaussian functions (for the two different height distributions), with the height determined as the difference between the centers of the two functions and the uncertainty

given as the quadrature addition of the two best-fit σ values. Table S1 lists all molecular layer thicknesses determined in the same way. To reflect the uncertainly in thickness, the values given in the main paper are rounded to the nearest 0.5 nm.
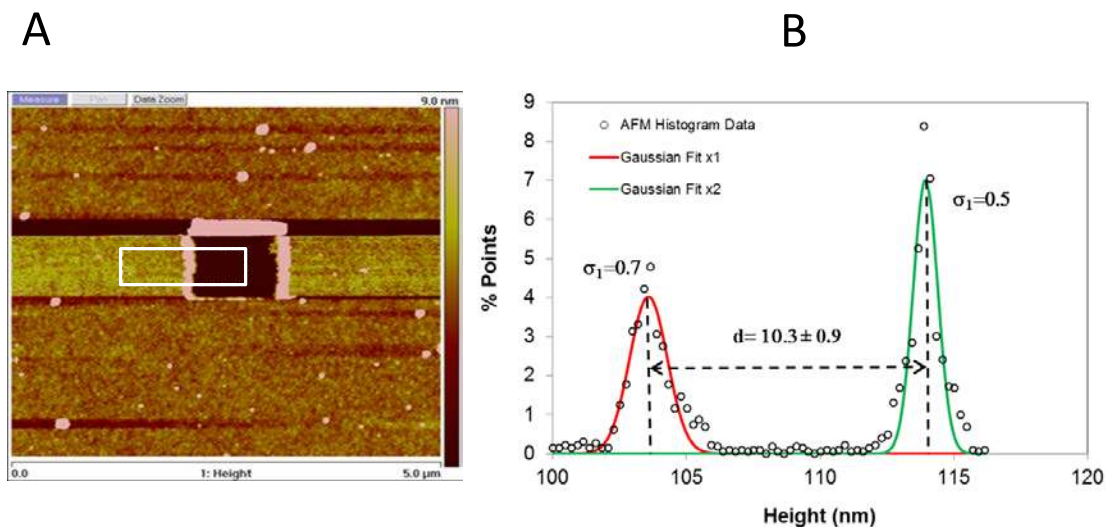
A   B

Figure S2. (A) 5 x 5 µm tapping mode image of a 1 x 1 µm "trench" made in a PPF/BTB layer using contact mode AFM. (B): histogram of heights determined within the white rectangle of the AFM image. Uncertainty in thickness is the quadrature addition of the two Gaussian σ values.

Table S1: BTB film derivatization conditions and corresponding film thicknesses (in nm) determined as shown in figure S2:

Derivatization Conditions	AFM Thickness
+0.4V to -0.4V, 1 scan	4.5 ± 0.7
+0.4V to -0.6V, 1 scan	5.2 ± 0.9
+0.4V to -0.4V, 2 scans	6.9 ± 0.6
+0.4V to -0.6V, 2 scans	8.1 ± 0.7
+0.4V to -0.4V, 4 scans	10.4 ± 0.8
+0.4V to -0.6V, 4 scans	12.8 ± 0.9
+0.4V to -0.6V, 6 scans	16 ± 1
+0.4V to -0.6V, 10 scans	22 ± 1

Layer thickness and integrity were confirmed by obtaining a STEM image of a completed PPF/BTB(10 nm)/e-C(10 nm)/Au(20 nm) junction sectioned by a focused ion beam. The image of figure S3 was obtained with a Hitachi S5500 STEM by Peng Li of the NINT microscopy facility. From top to bottom in the image are the PPF, BTB, e-C,

and Au layers of the junction plus an addition e-C layer added to protect the sample during ion beam sectioning.
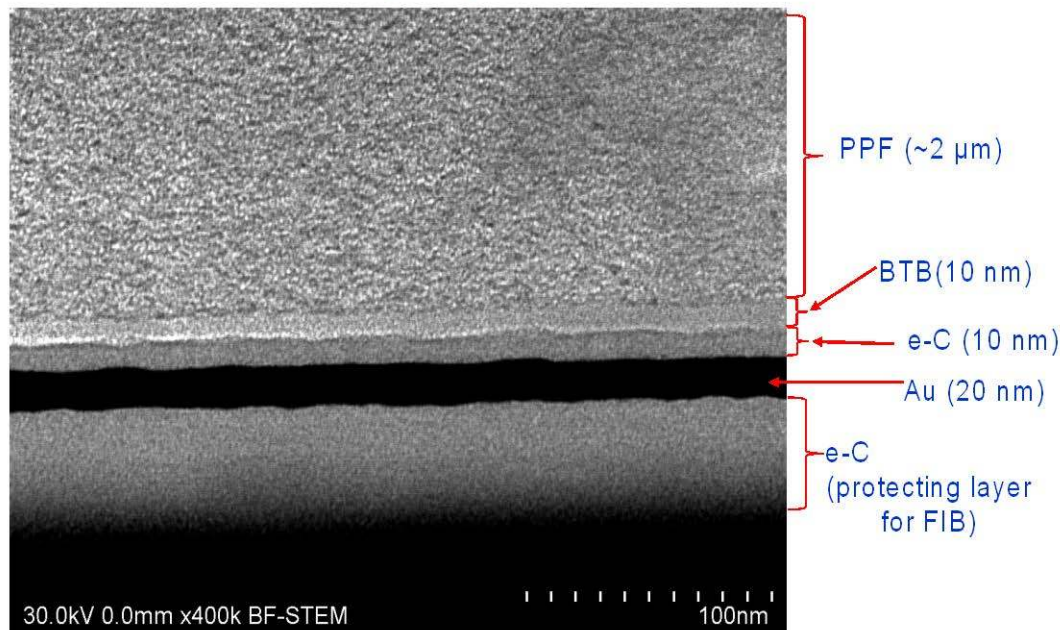

FIB/TEM of PPF/bisthiophenylbenzene/e-Carbon/Au:

PPF (~2 μm)
BTB(10 nm)
e-C (10 nm)
Au (20 nm)
e-C (protecting layer for FIB)

30.0kV 0.0mm x400k BF-STEM   100nm

Figure S3. A STEM image of PPF/BTB(10 nm)/e-C(10 nm)/Au(20 nm) junction obtained after sectioning with a focused ion beam (FIB). e-Carbon layer at bottom was applied preceding FIB sectioning to protect the junction layers.

4. Representative Current-Voltage results

As reported previously, relative standard deviations (*rsd*) for the current density measured for a series of independent molecular junctions made with the procedures outlined above are in the range of 10-20% (6, 7). An example for PPF/BTB/e-C/Au junctions is shown in figure S4A, which is an overlay of *JV* curves for seven different junctions with a BTB thickness of 22 nm. The *rsd* of *J* for the seven junctions varies from 8.3% at *V*=1 V to 19% at 0.5 V, with an average for this voltage range of 11.1%. The average for the -0.5 to -1.0 V range was 11.5% with a maximum of 15% at *V* = -1 V. Figure S4B is an expansion of the low voltage range for 13, 16, and 22 nm BTB junctions at 300K, showing the overlap of the 16 and 22 nm curves in the ±0.4 V range. The attenuation coefficient β for the 16-22 nm curves is (0.015 ± 0.005) nm^{-1} at $V = 0.3$ V, 0.037 ± 0.007 at $V = 0.5$ V, and $0.133 \pm .003$ at $V = 1.0$ V (see table S3). Stated errors are standard deviations of ten points determined for bias values centered on the stated voltage.
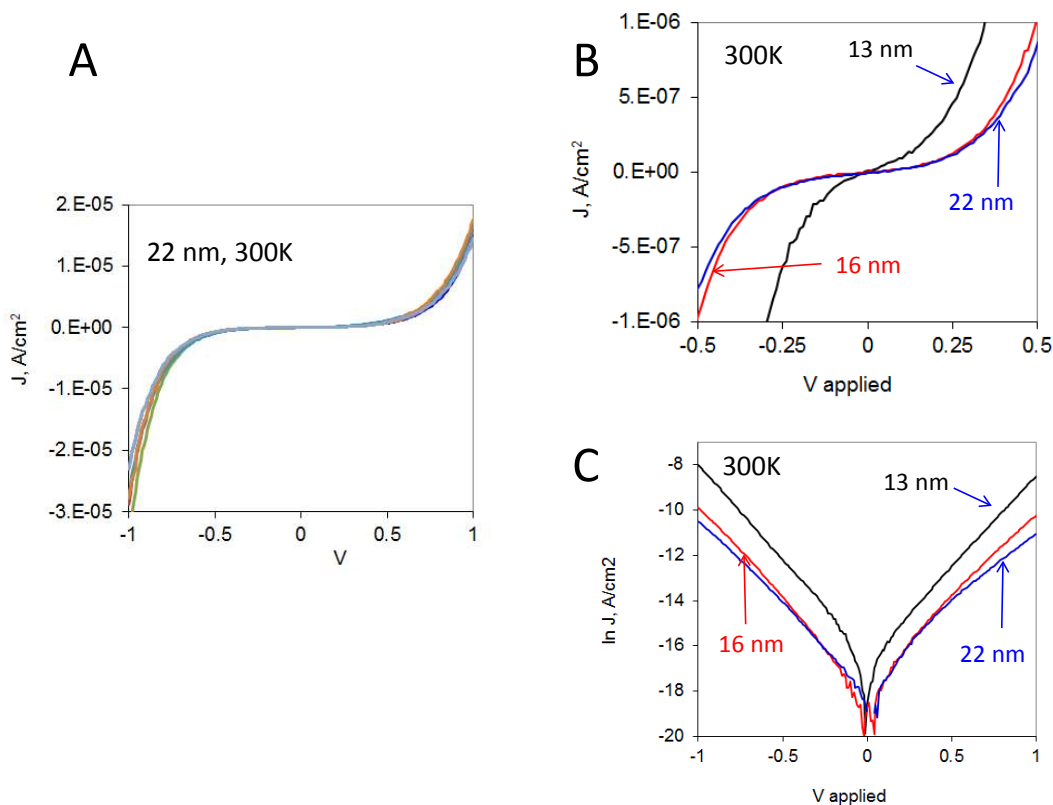
Figure S4. (A) Overlay of seven *JV* curves for independent PPF/BTB(22 nm)/e-C(10 nm)/Au(20 nm) junctions obtained at 300K (see supplemental text for statistics). (B) Magnified low bias region for 13, 16, and 22 nm BTB junctions at 300K, determined under identical conditions. (C) Same data as B, plotted with ln *J* axis.

5. Plots of ln*J* vs ln*V*

Plots of ln *J* vs ln *V* are useful for indicating mechanism, and several are shown in figure S5 for various BTB thicknesses and temperatures. A listing of the slopes of all cases examined is shown in Table S2 for both low and high bias ranges. The intercept of d(ln*J*)/d(ln*V*) at low *V* is 1.11 ± 0.14 for the 5-22 nm thickness range at 300 K, indicating ohmic behavior at low bias. This slope increases to 12-15 for d= 8.0, 10.5, and 22 nm as the bias is increased to ~5 V, indicating a major departure from ohmic behavior.
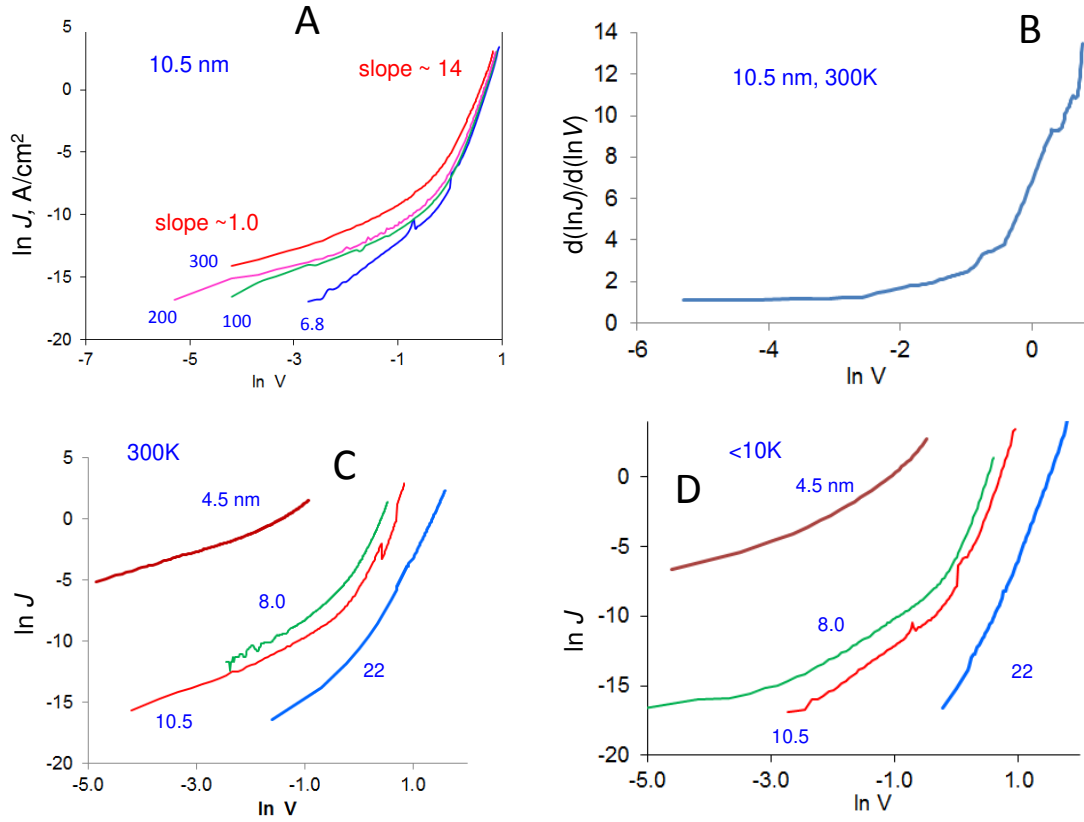
6

Figure S5. ln*J* vs ln*V* for several temperatures and BTB thicknesses. (A) 10.5 BTB thickness at indicated temperatures from 6.8 to 300 K. Approximate slopes are indicated, and a full listing is in Table S2. (B) slope of ln*J* *vs*. ln*V* plot vs ln*V* for 10.5 nm BTB at 300K; (C) Plots for four thicknesses at 300 K; (D) Plots for four thicknesses at <10 K.

Table S2: Slopes and intercepts of ln*J* *vs* ln*V* plots

	thickness	V range	slope @ 300K	slope, <10K		d, nm	intercept*
Low V:	4.5 nm	0.01-0.11	2.17	1.44		5.0	1.03
	8.0	0.01 - 0.10	1.92	0.91		7.0	0.96
	10.5	0.01-0.10	1.15	2.47		8.0	1.23
	22	0.8 - 1.3	3.97	7.71		10.5	1.03
						13	1.31
Hi V:	4.5	0.5-0.6	1.50	1.52		16	1.22
	8.0	1.7-1.8	13.20	13.80		22	0.97
	10.5	1.9-2.5	14.06	14.05		mean	1.11
	22	4.9-5.2	12.08	15.06		st. dev	0.14

* intercept of d(ln*J*)/d(ln*V*) at V=0 and 300 K

6. Attenuation coefficients (β) for various conditions

Table S3 lists β values with units of nm^{-1} derived from JV curves at various temperatures and bias ranges for the 8 thicknesses listed in table S1. Slopes of ln J vs d plots, many of which are shown in figure 2 of the main text, determined from least squares fits to 2-4 BTB thicknesses are listed. Values for high bias and thin BTB layers could not be determined because the current exceeded the instrumental limit (5 mA). Figure S4 shows that the 16 nm and 22 nm JV curves are indistinguishable in the range of ±0.4 V, with the result being a small β for the 12-22 nm range (0.015 at $V = 0.3$ V and 0.04 at $V = 0.5$ V)

Table S3. Attenuation coefficient β (nm$^{-1)}$ for various V and T

thickness range:	4-8 nm		8-16 nm		16-22 nm	
V @ 300K	β*	σ	β*	σ	β*	σ
0.3 V	2.86	0.32	0.81	0.17	0.015	0.005
0.5	2.4	0.44	0.79	0.17	0.037	0.007
1.0	2.89	0.32	0.88	0.17	0.13	0.003
1.5			0.95	0.17	0.15	
2.0			1.05		0.18	
3.0			0.75		0.28	
V @ 200K						
0.8	3.04		1			
1.5			0.9			
2.0			1.06			
V @ 100K						
0.8	3.06		1.12			
1.5			1.04			
2.0			1.18			
V @ 50K						
0.8	3.17		1			
1.5			1.14			
2.0			1.45			
V @ 6-8K						
0.5	3.02		0.65			
0.8	3.28		0.86			
1.5			1.03			
2.0			1.33			
mean	2.97		1.00		0.13	
st. dev.	0.266		0.197		0.097	
N	8		19		6	

* for 4.5-8 nm, β is the least-squares slope of 3-5 points of the plot of ln J vs junction thickness, and has units of nm^{-1}. σ is the standard deviation of the least squares slope. For 16-22 nm, β and σ were determined from 10 bias points surrounding the indicated bias.

7. Supplemental *JV* curves for *T* = 6-300 K range

Figure S6 shows *JV* curves at the indicated temperatures for 4.5 and 8.0 nm BTB junctions, obtained with the same conditions as Figures 3A and 3B of the main text. The T dependence for the 4.5 nm device is likely due to Fermi function broadening in the contacts, as proposed elsewhere (2, 14). Scans were independent of scan rate in the range 10-1000 V/s (excluding capacitive current when observed, see section 1), and could be repeated many times. In no case were effects of memory or fatigue observed, such as hysteresis or slow changes with repetitive scanning.
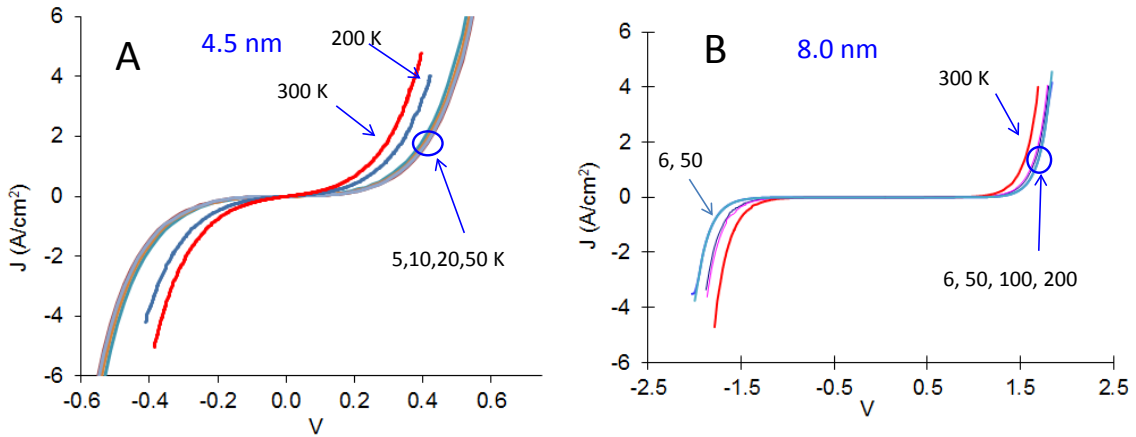

Figure S6. *JV* curves for 4.5 nm (A) and 8.0 nm (B) BTB junctions obtained at the indicated temperatures. Identical conditions as those for Figures 3A and 3B of the main text.

8. Variable Range Hopping (VRH) plots

The contribution of VRH to transport in disordered solids is characterized by linear plots of ln *J* vs $T^{-1/2}$ for one-dimensional Mott VRH or Efros-Shklovskii VRH, or linear ln *J* vs $T^{-1/4}$ for 3-dimensional Mott VRH. Such plots are shown for the 200-300 K range and three BTB thicknesses in figures S7A and S7B, along with a theoretical line calculated from standard VRH equations (15). Linearity was not observed for any of the experimental results in the conditions studied, and agreement between observations and VRH prediction was not observed for any physically reasonable parameters.
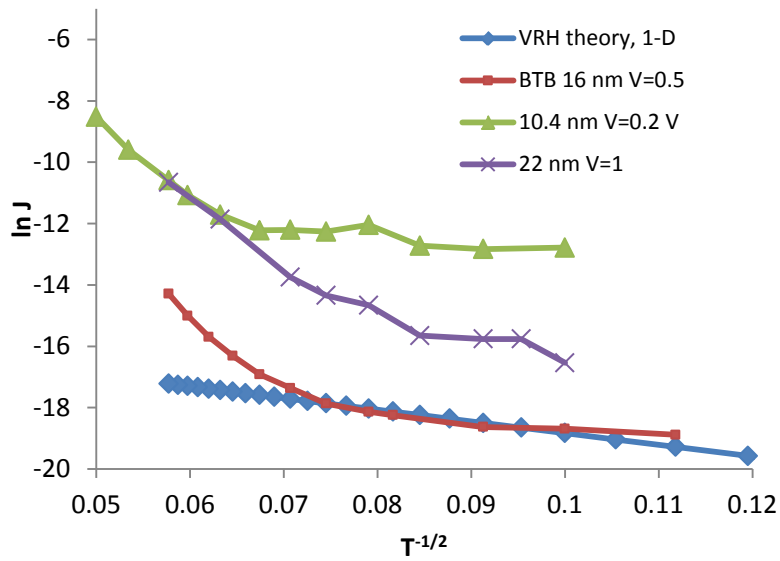
Figure 7A. Comparison of 1-dimensional Mott VRH theory with experimental observations. Theoretical line calculated for a prefactor of 3 x10^{-7} A/cm^2, localization length of 16 nm and density of states of 2 x 10^7 eV^{-1} cm^{-1}
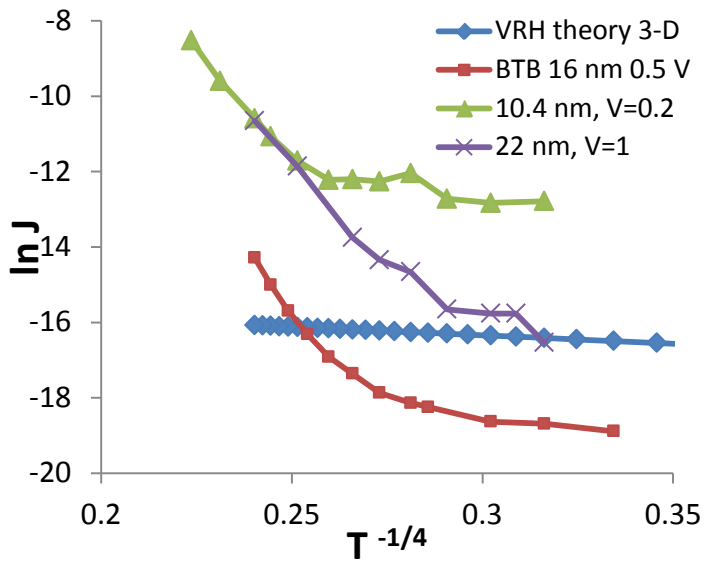

Figure S7B . Comparison of 3-dimensional Mott VRH theory with experimental observations. Theoretical line calculated for a prefactor of 3 x10^{-7} A/cm^2, localization length of 16 nm and density of states of 1.6 x 10^{20} eV^{-1} cm^{-3}

:

9. Activation barrier dependence on electric field

Classical Poole-Frenkel transport between coulombic traps is given by (16-18):

$$J_{PF} = q\,\mu\,N_o\,E\,\exp\left(\frac{-q\Phi}{kT}\right)\exp\left[\left(\frac{q^3 E}{\pi\varepsilon_o\varepsilon}\right)^{\frac{1}{2}}\frac{1}{kT}\right]$$

$$\ln\left[\frac{J}{E}\right] = \ln(q\,\mu\,N_o) - \frac{\Phi}{kT} + \left[\frac{q^{3/2}}{(\pi\varepsilon_0\,\varepsilon)^{1/2}\,kT}\right]E^{1/2}$$

where μ is mobility of a detrapped carrier, N_o is the number of traps, E the electric field, ϕ is the trap depth, k the Boltzmann constant, and $\varepsilon_o\varepsilon$ is the dielectric constant. These equations predict that a plot of $\ln(J/E)$ vs $E^{1/2}$ should be linear with a slope that is dependent inversely on temperature. Furthermore, a standard Arrhenius plot of $\ln J$ vs $1/T$ should have a slope of:

$$E_a = -\text{ slope of } \ln J \text{ vs } 1/T = -q\,\Phi/k + \left[\frac{q^{3/2}}{(\pi\varepsilon_0\,\varepsilon)^{1/2}\,k}\right]E^{1/2}$$

Therefore, the slope of a plot of the apparent activation barrier E_a in eV vs $E^{1/2}$ is equal to $(q/\pi\varepsilon_o\varepsilon)^{1/2}$, which is 0.289 meV cm$^{1/2}$ V$^{-1/2}$ for $\varepsilon = 6.9$, as determined from junction capacitance. Figure S8A shows E_a vs $E^{1/2}$ for the indicated thicknesses of BTB in the temperature range 200-300 K. The lines are least-squares fits for the 16 and 22 nm data. The slopes and intercepts are as follows: 16 nm: $y = 0.221x + 350$ ($R^2 = 0.974$); 22 nm: $y = 0.197x + 296$ ($R^2 = 0.967$).

Figure S8B shows Poole-Frenkel plots for a 22 nm BTB junction at four temperatures from 5.8 K to 300 K. According to the equations above, the slopes should vary by a factor of 50 (300/6) in this range, yet in fact vary by only a factor of 1.3.
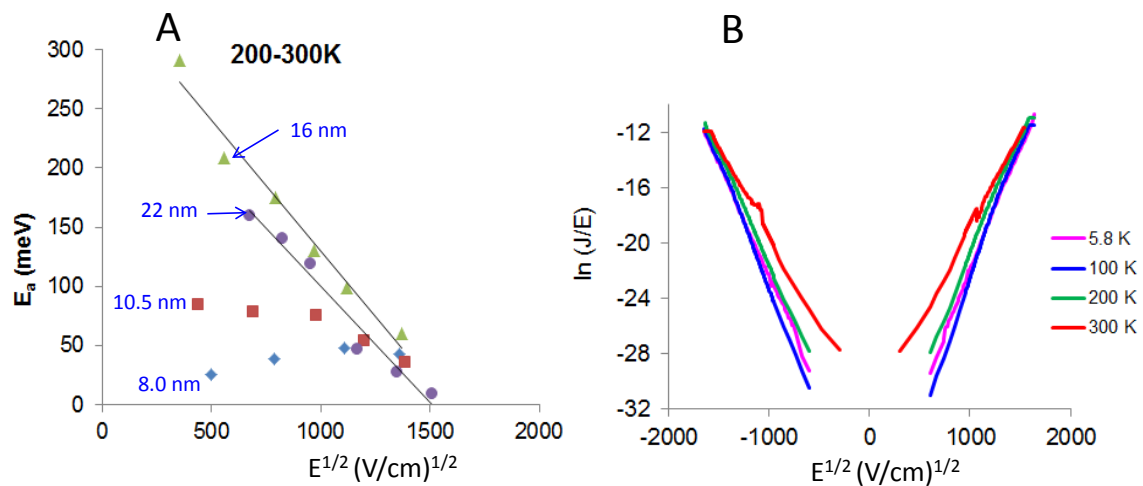
Figure S8. (A) Observed activation energies E_a from Arrhenius plots in the 200-300 K range plotted vs the square root of the electric field. Labels with each set of points indicate the BTB thickness. Lines are least-squares fits to the data for 16 and 22 nm. (B) ln(J/E) vs $E^{1/2}$ curves for 22 nm BTB junctions at the four temperatures indicated.

References:

1. Bergren AJ, Harris KD, Deng F, & McCreery R (2008) Molecular Electronics using Diazonium-Derived Adlayers on Carbon with Cu Top Contacts: Critical Analysis of Metal Oxides and Filaments. *J. Phys. Condens. Matter* 20:374117.
2. Bergren AJ, McCreery RL, Stoyanov SR, Gusarov S, & Kovalenko A (2010) Electronic Characteristics and Charge Transport Mechanisms for Large Area Aromatic Molecular Junctions. *J. Phys. Chem. C* 114:15806-15815.
3. Bonifas AP & McCreery RL (2010) "Soft" Au, Pt and Cu contacts for molecular junctions through surface-diffusion-mediated deposition. *Nature Nanotechnology* 5(8):612-617.
4. Fave C*, et al.* (2007) Tunable Electrochemical Switches Based on Ultrathin Organic Films. *J. Am. Chem. Soc.* 129(7):1890-1891.
5. Mahmoud AM, Bergren AJ, Pekas N, & McCreery RL (2011) Towards Integrated Molecular Electronic Devices: Characterization of Molecular Layer Integrity During Fabrication Processes. *Adv. Funct. Mater.* 21(12):2273-2281.
6. Sayed SY, Fereiro JA, Yan H, McCreery RL, & Bergren AJ (2012) Charge transport in molecular electronic junctions: Compression of the molecular tunnel barrier in the strong coupling regime. *Proceedings of the National Academy of Sciences* 109(29):11498-11503.
7. Yan H, Bergren AJ, & McCreery RL (2011) All-Carbon Molecular Tunnel Junctions. *J. Am. Chem. Soc.* 133(47):19168-19177.
8. Kumar R, Pillai RG, Pekas N, Wu Y, & McCreery RL (2012) Spatially Resolved Raman Spectroelectrochemistry of Solid-State Polythiophene/Viologen Memory Devices. *J. Am. Chem. Soc.* 134(36):14869-14876.
9. Ru J, Szeto B, Bonifas A, & McCreery RL (2010) Microfabrication and Integration of Diazonium-Based Aromatic Molecular Junctions. *ACS Applied Materials & Interfaces* 2(12):3693-3701.
10. McCreery R, Wu J, & Kalakodimi RJ (2006) Electron Transport and Redox Reactions in Carbon Based Molecular Electronic Junctions. *Phys. Chem. Chem. Physics.* 8:2572-2590.
11. Ranganathan S, McCreery RL, Majji SM, & Madou M (2000) Photoresist-Derived Carbon for Microelectrochemical Applications. *J. Electrochem. Soc.* 147:277 - 282.
12. Kumar R, Yan H, McCreery RL, & Bergren AJ (2011) Electron-beam evaporated silicon as a top contact for molecular electronic device fabrication. *Physical Chemistry Chemical Physics* 13(32):14318-14324.
13. Anariba F, DuVall SH, & McCreery RL (2003) Mono- and Multilayer Formation by Diazonium Reduction on Carbon Surfaces Monitored with Atomic Force Microscopy "Scratching". *Anal. Chem.* 75:3837-3844.
14. Poot M*, et al.* (2006) Temperature Dependence of Three-Terminal Molecular Junctions with Sulfur End-Functionalized Tercyclohexylidenes. *Nano Lett.* 6(5):1031-1035.
15. Eui Yun J*, et al.* (2012) Fibers of reduced graphene oxide nanoribbons. *Nanotechnology* 23:235601.
16. Simmons JG (1967) Poole-Frenkel Effect and Schottky Effect in Metal-Insulator-Metal Systems. *Physical Review* 155(3):657-660.
17. Sze SM (1981) *Physics of Semiconductor Devices* (Wiley, New York) 2nd Edition Ed.
18. Vodenicharov CM & Vodenicharova MB (1980) Schottky and Poole-Frenkel Mechanisms of Conductivity in Thin-Film Me-GeS-Me Systems. *Physica Status Solidi (A)* 57(2):483-487.